Continental Shelf Research 34 (2012) 30–40

Contents lists available at SciVerse ScienceDirect

Continental Shelf Research

journal homepage: www.elsevier.com/locate/csr

Research papers

Analysis of imposing tidal dynamics to nested numerical models

Ivica Janeković *,[1], Brian Powell

University of Hawai'i at Mānoa, Department of Oceanography, Marine Sciences Building, 1000 Pope Road, Honolulu, HI 96822, USA

ARTICLE INFO

Article history:
Received 21 July 2011
Received in revised form
17 November 2011
Accepted 30 November 2011
Available online 9 December 2011

Keywords:
Internal tides
Nested models
Boundary conditions
ROMS model
Hawaii

ABSTRACT

Tides often play an important role in the circulation of coastal and shelf environments. In numerical modeling, high-resolution models are used for these regions requiring that they be nested in coarser models with properly specified tidal boundary conditions. In this paper, we examine two, one-way nesting methods for specifying the combined baroclinic and barotropic tides to a child model: (i) specifying spatially interpolated boundary values from the outer model at a specified interval; and (ii) using the same boundary conditions as (i), but fitting and removing the tidal harmonics from the boundaries and providing the harmonics as separate forcing. We compare these methods in two regions: an idealized seamount experiment where baroclinic tides are generated outside of and propagate into the nested domain; and, a realistic case of the Hawaiian archipelago with strong barotropic tides with significant energy conversion to the baroclinic tide both inside and outside of the nested domain. In all cases, we find that there is significant improvement in the tidal dynamics by removing the tides from the boundary conditions and using a separate tidal forcing as compared to simply prescribing the boundary conditions. Furthermore, because many numerical models use temporal linear interpolation for boundary conditions at each time-step, if the tidal function is not specified separately, the amplitudes are significantly reduced and – more importantly – energy is aliased at higher frequencies. These findings are applicable to any tidally energetic region (particularly shelf and coastal systems) and become more significant with nonlinear interaction between tidal constituents.

1. Introduction

Dynamical features of the ocean are found on a variety of spatial and temporal scales: from O(10–1000 km and days) for off-shore currents, fronts and eddies to shelf and coastal dynamics affected by land and bottom boundaries at O(1 m–10 km and minutes). Most numerical models cannot resolve the full range of dynamics with a single grid and models with high resolution dynamics (“child”) require nesting into a coarser resolution (“parent”) model. The parent prescribes the flow to the child via lateral boundary conditions (BC). For the hydrostatic primitive equations, the BC are an ill-posed problem (Oliger and Sundstrom, 1978; Bennett and Kloeden, 1978; Bennett, 1992) because there does not exist a complete set of BC that guarantee a unique and stable solution. Different types of applied BC or even small changes along them can lead to significantly different solutions inside the child domain (Palma and Matano, 1998; Marchesiello et al., 2001; Dinniman and Klinck, 2002; Oddo and Pinardi, 2008).

There are two primary choices for the child nest: “one-way” in which data from the parent is provided to the child at the boundaries without the child providing information about the flow back to the parent (e.g., Penven et al., 2006; Mason et al., 2010); or, “two-way” which allows dynamical feedback from the child back to the parent (e.g., Debreu and Blayo, 2008). Either scheme can be used in either “online” (when both the parent and child grids are integrated together, time-stepping between each other) or “offline” (when the parent is integrated, the BC are generated and the child is integrated) modes.

In many regional shelves and seas, tides are a fundamental component of the circulation and cannot be ignored; unfortunately, many of the currently available global ocean solutions do not currently include the tides, so the regional models must provide the tidal dynamics. In regions containing both barotropic and baroclinic dynamics, special consideration must be given to how the tides are imposed on the BC for the nested child. The child contains increased resolution of the topographic features, which may steer or slow the tidal flow. Baroclinic tides may be generated remotely and are propagated into the child or may be generated within the child and should not reflect at the boundaries. The fundamental problem with any nesting is that features that occur at time-scales not well resolved by the boundaries are

* Corresponding author.
E-mail addresses: ivica@soest.hawaii.edu (I. Janeković), powellb@hawaii.edu (B. Powell).
[1] On leave to Institute Rudjer Boskovic (ivica@irb.hr)

0278-4343/$ - see front matter © 2011 Elsevier Ltd. All rights reserved.
doi:10.1016/j.csr.2011.11.017

lost. Furthermore, depending upon the temporal interpolation of the boundaries, energy may be introduced at incorrect frequencies.

Generating tidal BC varies depending upon the model application and region. In many cases, the barotropic tides are imposed as a perturbation to the free surface BC, and (in the case of tidal flow) to the barotropic velocity. Commonly, the tidal data are generated from a global tidal solution such as the Oregon State University TOPEX/Poseidon Global Inverse Solution (TPXO) (Egbert and Erofeeva, 2002). For regional tidal data some generate the BC by solving an inversion problem using available tidal observations (Janeković et al., 2003; He and Wilkin, 2006; Janeković and Sikirić, 2007). As resolution of models increase and more shelf and shore interactions are resolved, further nesting is required, and determining of optimal tidal BC may magnify into a significant problem.

In this paper, we investigate two, one-way nesting methods for specifying the combined baroclinic and barotropic tides to a child model: (i) through time-dependent boundary conditions generated by the parent; or (ii) using the same boundary conditions as (i), but removing the barotropic tides and specifying them spectrally. Neither method is new; however, we present a detailed analysis of the two methods that reveals the significant limitations of (i), especially in regions of strong baroclinic tides.

To investigate those differences we present two cases: an idealized sea-mount that remotely generates internal tides that propagate into the child nest, and a realistic case around the island of O'ahu in Hawai'i with internal tides generated both inside and outside the child nest. These results are applicable to many regions of the oceans where strong baroclinic tides exist (Simmons et al., 2004), such as Aleutians Islands/Trench, Bay of Biscay, Drake Passage, South and North Fiji basin, Kyushu/Palu Ridge, Macquarie Ridge, Luzon Strait, Kuril Island, etc.

Furthermore, from a state estimation perspective, the choice of applying the boundary conditions has particular significance. When using an advanced state-estimation method, such as 4D-variational (e.g., Le Dimet and Talagrand, 1986) or ensemble Kalman filtering techniques (e.g., Evensen, 1994), the boundaries are often part of the control vector. Because the barotropic tides are deterministic, altering the boundary conditions to influence the tides is a potentially adverse side-effect of the assimilation. By separating the tidal from the time-dependent boundaries, the assimilation schemes may improve the density and flow structure while leaving the tides unaffected.

2. Methodology

In this paper, we compare methods of specifying the BC to a child nest, and we examine them in the presence of barotropic and baroclinic tides. We examine two methods for one-way nesting: (i) specifying the parental values at specified interval; and (ii) using the same boundary conditions as (i), but extracting the barotropic tides and specifying them as spectral forcing to the model. For method (i), values from the parent solution are spatially interpolated to the child boundary at selected time intervals. For method (ii), the values from the parent solution are also interpolated to the child boundary at a selected time interval, but each barotropic field (free-surface and depth-average velocity) are used to fit the known tidal signals using a package such as `t_tide` (Pawlowicz et al., 2002). This tidal fit reproduces the precise tidal function from the given samples. As long as enough samples are provided for each tidal cycle (see Appendix), the tidal signal will be reconstructed. The tidal signals are then removed from each barotropic field in the BC and the coefficients of the tidal signal are then prescribed to the model separately. It is important to note that a time-series of enough length is required to resolve tidal signals that are very close in frequency (such as S_2 and K_2). Furthermore, the baroclinic component of the BC are not altered. This is because the baroclinic tides contain quasi-random phase-shifts due to changes in oceanic density that affect the propagation of the baroclinic waves (Chavanne et al., 2010).

The key component of method (ii) is that the same fields from the same sampling period of method (i) are used, but the tidal spectrum is fit to the data and then removed from the BC. The spectral coefficients are then specified to the model separately, such that it can reproduce the tidal signal at any point in time.

We used the Regional Ocean Modeling System (ROMS), a 3D hydrostatic, nonlinear, free surface, s-coordinate, time splitting finite difference primitive equation model (Shchepetkin and McWilliams, 2005, 2009). More detailed description of the model numerical schemes can be found at ROMS webpage (http://www.myroms.org). In all cases, the child nest used clamped baroclinic BC and Chapman (1985) for free surface while modified Flather type (Marchesiello et al., 2001) for barotropic momentum BC. ROMS allows for tidal forcing to be specified via a spectral file and the perturbation to the free-surface and barotropic velocities separately in time.

For all experiments in this paper, we designate the child cases by the frequency at which the boundaries are applied in minutes. For example, C20 and C180 designate method (i) cases where the child used BC from the parent at 20 and 180 min intervals, respectively. Method (ii) cases are designated with a suffix "t": C180t.

3. Idealized rectangular case

The first experimental case includes a seamount to generate baroclinic tides such that it approximates the actual regions of interest. We use a rectangular basin of 1° size with a spatial resolution of 1 km and 20 vertical layers having increased resolution in the surface region. The depth of the basin is 500 m except at the seamount, which is shown in Fig. 1. The child nest (Fig. 1) has horizontal resolution of 200 m with the same vertical coordinates as the parent. The parent model is forced only by an M_2 tide at the free surface along the western boundary with an amplitude of 50 cm. Walls are imposed on the northern and southern parent boundaries with strong, linearly increasing,

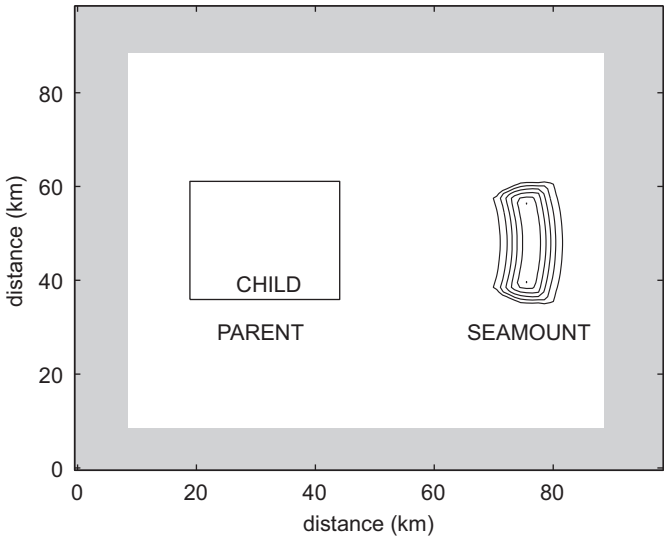

Fig. 1. Idealized rectangular basin setup; parent grid has resolution of 1 km, while child grid has a resolution of 200 m. Shaded region represent region of sponge layer and contours of seamount are plotted every 50 m from 450 m (bottom is at 500 m) to 250 m depth (200 m is the top of the seamount).

sponge layers across 10 km in order to prevent reflected energy back into the domain. Along the eastern boundary, values for temperature, salinity, and velocity are strongly nudged back towards the quiescent state as we do not want retroflections from the eastern flank of the seamount. The ocean is started from rest with a stably stratified density and a pycnocline at 150 m.

In terms of barotropic to baroclinic energy conversion one of the important parameters is the slope factor (Garrett and Kunze, 2007) between bathymetry and internal waves, given by

$$\gamma = \alpha \left(\frac{\omega^2 - f^2}{N^2 - \omega^2} \right)^{-1/2}, \quad (1)$$

where α is the bathymetric slope, ω is the tidal angular frequency, f is the Coriolis parameter, and N is the buoyancy frequency. A seamount is classified as supercritical if $\gamma > 1$ and subcritical if $\gamma < 1$ (Garrett and Kunze, 2007). For this experiment, $\gamma = 1.2$, such that it is weakly supercritical. We can expect conversion of barotropic to baroclinic energy as well as internal wave dynamics to occur in a similar way as in Balmforth and Peacock (2009). The scope of this paper is not to fully analyze barotropic to baroclinic conversions for different topography, density or frequencies (e.g., Qian et al., 2010; Lorenzo et al., 2006) but to provide insight into the capabilities, limits, possible errors when using one-way nested approach in such a demanding environment.

3.1. Simple f-plane case

The nesting procedure is first examined in the idealized setup using an f-plane. The parent model was integrated for 10 days, and its results were used to generate the BC for the child every 20 min. Four sets of BC are generated via subsampling in time: C20, C60, C120, and C180. For method (ii), the 180 min BC were used to create the spectral tidal forcing: C180t. It is important to note that to resolve the full spectrum of the known barotropic tide, one need only sample at least two points in its period; hence, for M_2, the boundaries are required at least every 6.2 h (see Appendix for details). Thus, an important conclusion is that to properly capture the full barotropic tidal dynamics, frequent BC are not required when using method (ii).

We chose these subsampling frequencies as approximate even multiples of both the M_2 cycle and synodic day. From the practical point of view, it is rarely possible to save the parent model results at 20 min interval. The aim is to compare the various effects caused by different frequency BC with that of method (ii) using coarse sampling and spectral tides. We consider the tidal circulation (both barotropic and baroclinic) from the parent as truth, which was saved every 20 min. We expect that the barotropic tide – expressed as displacement of the free surface and vertically averaged velocity – is consistent between the parent and child. The C20 case matches the parents tidal signal quite well; however, as the frequency of the BC is reduced, the amplitude of the child free-surface tidal expression is affected as best illustrated in the C180 case (Fig. 2, the C60 and C120 cases are not shown for clarity). As ROMS linearly interpolates the BC in time, the tide is broken into discrete 3 h measures with a linear fit between.

Worse is that this linear interpolation introduces aliased energy at higher frequencies (Fig. 3) into the child domain. This is not surprising as an analytical evaluation of sampling a known signal and linearly interpolating is known to generate higher frequency aliasing as shown in Appendix. To completely avoid this consequence in a nested grid that does not use spectral tides would require BC specified at each time-step of the child model: an impractical and costly exercise.

On the other hand, using 3 hourly BC for the relatively slowly evolving baroclinic component in combination with barotropic specified in spectral space (C180t) gives results superior to C20 case when compared against parent solution for the same location and barotropic signal. The root mean squared error (RMSE) between the parent and child at the same location for the free surface over the final five M_2 cycles is found to be 0.8, 1.1, 3.2, 7.2 and 0.6 cm for C20, C60, C120, C180 and C180t cases, respectively. RMSE between the parent and the child for the barotropic velocity are 0.12, 0.15, 0.45, 0.98 and 0.09 cm/s. The C180t is an order of magnitude improvement over the C180 case, and is similar to the C20 case; however, the C180t reduces the disk storage requirements by a factor of nine from C20.

In addition to the barotropic tides, it is important to maintain the baroclinic tide within the child. One would expect the C180 and C180t cases to have similar baroclinic structure as a result of the same update frequency through the BC. We examine the east–west baroclinic energy flux, given by

$$\mathcal{F} = \int_{-\mathcal{H}}^{0} \langle p' u' \rangle_\theta \, d z, \quad (2)$$

where $\langle \cdot \rangle$ denotes the expectation (in this case the time mean) over a tidal period, p' is pressure perturbation given by $p' = p - \langle p \rangle_\theta$, and u' is baroclinic velocity perturbation given by $u' = u - \langle u \rangle_\theta$ (Nash et al., 2005; Carter et al., 2008). F is computed at 20 min time interval for the final five tidal cycles across a vertical transect through the middle of child nest as the baroclinic flow propagates west from the seamount. The RMSE between the child and parent time series of F is scaled by the temporal mean of

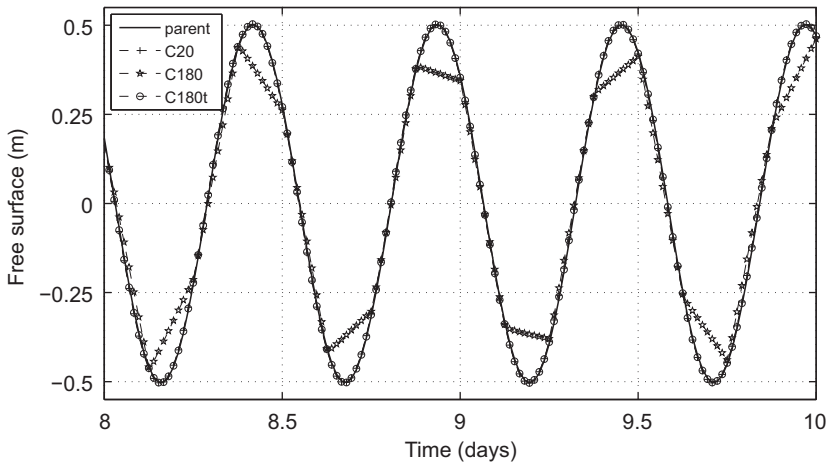

Fig. 2. Free surface at the center point of the child grid as given by the parent solution (solid line), C20 case (+), C180 case (stars) and C180t case (circles).

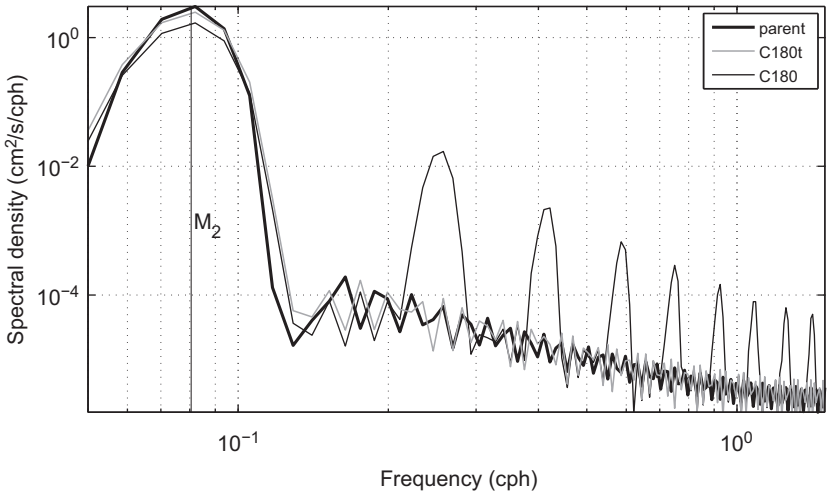

Fig. 3. Spectral density from time-series of free surface at the center point of the child grid from the parent solution (black thick line), C180 (light gray thin line), and C180t (black thin line).

the parent's *F*. This calculation yields the percent decrease in baroclinic energy for each child experiment. We find the decrease in energy to be 6%, 6%, 9.2%, 17.3% and 16.9% for C20, C60, C120, C180 and C180t cases, respectively. Although the barotropic tide is well captured in method (ii), the baroclinic energy was still reduced by 17% as a function of the temporal resolution.

To understand the significance of this baroclinic energy, we examine how the total kinetic energy compares inside the child model to the parent. Calculating the total kinetic energy for the final five M_2 cycles, we find the percent decrease from the parent to be 7.0%, 20.3%, 21.0%, 37.6%, and 7.7% for the C20, C60, C120, C180 and C180t cases. Although the baroclinic energy was reduced in method (ii) by 11% more than in C20 case, it is a significantly smaller portion in total kinetic energy budget, where method (ii) showed similar results as C20.

3.2. β-Plane *with zonal flow case*

To better approximate a regional sea, we examine a case using a β-plane centered at 21°N with a westward, zonal flow at the eastern boundary of the parent grid. This flow is opposite to the barotropic tidal propagation and is characterized with core velocity of 50 cm/s at the surface and the middle of eastern boundary. Using a *sine* decay function, the flow is gradually reduced to zero at the bottom and at the northern and southern boundaries. As shown in Eq. (1), the slope parameter will now vary meridionally on the seamount with the changing *f*. In order to introduce density field variations in the zonal flow, daily, stably stratified random perturbations are added to the temperature field above the 150 m thermocline at the eastern boundary. This provides a temporally and spatially varying density field that is advected into the domain to represent flow interaction with tidal dynamics in regions of significant internal wave generation. Generating time variability in the density field is necessary for internal waves to have varying ray paths and surface at different locations (Chavanne et al., 2010). After 20 days of integration, a large, cyclonic eddy formed in the western lee of the seamount and propagated westward through the child nest presenting an ideal test case (Fig. 4).

For these analysis, we used a 17 day period ($\sim$33 M_2 cycles) to compare the results of various BC. As in the previous case, the barotropic free surface was favorably resolved by the C180t. The RMSE values for free surface are 0.2, 0.8, 3.2, 7.1 and 0.6 cm for the C20, C60, C120, C180 and C180t cases, respectively. This

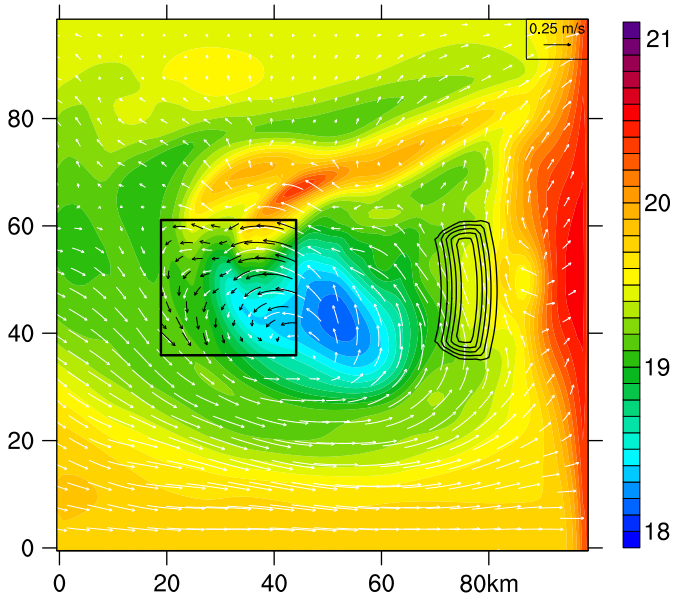

Fig. 4. Sea surface temperature and velocity snapshot from the parent and child C180t experiment nearly 24 days into the integration. Black lines mark child nested domain, black arrows surface velocities from C180t simulation and white arrows from parent.

results in a $\sim 12\times$ improvement from the C180t case over the C180. The RMSE of barotropic velocity is 0.39, 0.41, 0.59, 1.05 and 0.39 cm/s.

For the baroclinic flux, the percent decrease is found to be 3.4%, 3.5%, 6.2%, 8.4%, and 8.5% for the C20, C60, C120, C180 and C180t cases. These values are lower than the previous example because the flow now contains a meridional component. Baroclinic flux reductions across a zonal plane are found to be 2.4%, 2.6%, 3.4%, 5.8% and 6.1%. For baroclinic tidal flux, more frequent updates of the BC are more important than in barotropic case simply because the tidal spectral part is not as well defined. Depending upon the region of interest, it may be necessary to impose the BC more frequently than 3 hourly, but the advantage of method (ii) is obvious.

As with before, the reduction in baroclinic energy flux is a relatively small portion of total energy. Comparing the percent of total kinetic energy decrease yields a similar pattern as before;

9.4%, 11.8%, 19.6%, 30.8%, and 11.7% for C20, C60, C120, C180 and C180t with respect to the parent. It is obvious that BC specified every 2 h can underestimate total kinetic energy inside the child model by 20% and it is even worse in the case of every 3 h; however, method (ii) helps to reduce these problems.

Although we focus on the tidal energy, it is important that the advective flow is not affected by the choice of BC as the background flow is on the inertial frequency ($\sim$35 h period for 21°N). To compare the strength of the inertial flow, we examine the eddy kinetic energy (EKE) from each case with the parent. During the period in which the eddy propagated from the parent to the child, we compared the reduction in EKE for each child. It should be noted that because the eddy is across the parent/child boundary, the child is not allowed to fully develop the eddy at the higher resolution, which results in some loss of energy. For the present experiment, the loss in EKE is 1.5%, 1.4%, 1.2%, 0.4%, and 0.5% for the C20, C60, C120, C180 and C180t cases. In this case, the more frequent update limits the child from evolving the features at the higher-resolution.

The conclusion is that one should choose BC appropriate for the baroclinic dynamics of interest and impose the barotropic tides spectrally to improve the total solution and avoid aliasing energy at higher frequencies.

4. Hawaiian case

For the idealized case, method (ii) with adequate temporal resolution for the baroclinic structure was shown to be ideal; however, this must be examined for one-way nested applications in regions of strong tidal dynamics. The Hawaiian islands provide a perfect test-case for these methods. The Hawaiian archipelago sits in the deep Pacific basin near the southern part of the northern Pacific, sub-tropical gyre. Despite their small size, the islands exert a significant influence upon the climate of the Pacific (Xie et al., 2001). In addition, the M_2 tidal propagation is nearly perpendicular to much of the island ridges creating regions of strong barotropic to baroclinic tidal conversions. These baroclinic internal waves form a significant component of the island circulation (Merrifield and Holloway, 2002; Carter et al., 2008). Around the islands, the baroclinic tidal circulation can account for nearly 50% of the mean flow, and nearshore, the currents change direction every 12 h with the M_2 tide. Furthermore, because of the steep slope of the island seamounts, the topography can be complex, which requires fine-scale models near the islands. It is estimated that the total barotropic M_2 tide loses energy of the Hawaiian archipelago is 18–25 GW (Zaron and Egbert, 2006). Near the island of O'ahu, Carter et al. (2008) estimated a loss of 2.7 GW from the M_2 barotropic tide, of which, 163 MW is dissipated by bottom friction, and 2.3 GW is converted into internal tides. The majority of this internal tide energy (1.7 GW) is radiated out of the Hawaiian domain, while 0.45 GW is dissipated close to the generation regions. Furthermore, Carter et al. (2008) found that a 1 km resolution model provided a roughly 40% greater barotropic tidal dissipation rate than in a previous study with 4 km resolution (Merrifield and Holloway, 2002) suggesting a benefit of high resolution coastal simulations. Obviously, nested models in such regions that have scales of energy from the basin-scale down to nearshore, tidally dominated features must be assembled with care.

4.1. Model setup

To examine the Hawaiian region, we use a model of the archipelago that is characterized with constant horizontal resolution of 4 km and 30 vertical s-levels with increased resolution in the surface region. Inside the Hawaiian domain (parent model), we nest a child model around the southern edge of O'ahu with a curved and stretched domain having spatial resolution varying from 500 m in the coastal region to 2500 m in the deeper ocean (Fig. 5, bottom). In this model configuration, the coastal and reef shelves of the island are of high resolution with coarser resolution in the deeper regions to maintain a reasonable model time step to enforce stability. The southern region of O'ahu is tidally interesting for two reasons: the dominant internal waves are generated to the northwest of the island with a significant portion of the energy trapped along the isobaths and propagating around the southern edge and the generation of weaker internal waves at Penguin Bank and on the southeastern tip of O'ahu. For this experiment, only the M_2 tidal forcing is applied using data from the TPXO regional inverse tidal solution for Hawai'i. To focus our examination on the effects of nesting on tidal dynamics, we use a stably stratified, quiescent ocean with a vertical profile based upon climatology. This setup provides a practical example of the issues of nesting. Due to the large-size of the parent grid, it is not feasible to save data every 20 min in order to create BC for a child grid. Even at 1 h, the files generated require tens of gigabytes of storage for each 30 day period. So, a method that minimizes the frequency of BC while maintaining the tidal structure and flow is paramount.

4.2. Model results and validation

Fig. 5 shows the barotropic M_2 amplitude from the final 20 cycles of the 30 day integration. By comparison, the higher resolution (1/60°) TPXO regional tide solution does not contain any internal tide signature as it is a 2D barotropic model. In regions where internal waves are significant, these global tidal solutions are inappropriate for driving small-scale models, and regional models that include tidal dynamics are required. With a parent model that is generating significant baroclinic energy in the presence of strong barotropic tides with complex bathymetry, our interest lies in how to prescribe the flow to a nested, higher-resolution model. For this experiment, C60, C180, and C180t BC are generated. Direct comparison with the parent solution is no longer feasible as in the previous examples because the parent and child grids contain differently resolved bathymetries with varying child resolution, which affect the propagation of the tides. Instead, we utilize three long-term sets of observations taken from Hawaiian waters: (i) Honolulu Tide Gauge Station (Fig. 5, red dot); (ii) horizontal velocities from moored Acoustic Doppler Current Profilers (ADCPs) taken in 1996–1997 (labeled CM1); and (iii) horizontal ADCP velocities from 2010 (labeled CM2). Although this experiment uses only M_2 tidal constituent, neglects nonlinear interactions with other tidal constituents, and uses a climatological vertical density profile, it is still capable of reproducing major M_2 tidal structure. This can be confirmed by comparing the barotropic tides to the local tide gauge station. In order to quantify differences between different solutions and tide gauge, we define the inphase-quadrature plane distance as

$$\mathcal{D} = \sqrt{(\mathcal{A}_o \cos(f_o) - \mathcal{A}_m \cos(f_m))^2 + (\mathcal{A}_o \sin(f_o) - \mathcal{A}_m \sin(f_m))^2}. \quad (3)$$

$\mathcal{A}_o$ and $\mathcal{A}_m$ are, respectively, the observed and modeled M_2 amplitudes and f_o and f_m their phases. The distance, $\mathcal{D}$, accounts simultaneously for differences in amplitude and phase. As shown in Table 1, the parent underestimates the M_2 amplitude by 16% and is phase shifted forward by 29°. This is a result of the coarsely defined 4 km bathymetry as it moves into a shallow harbor protected by a small island. As the parent model contains bathymetry that is too deep, the barotropic tides will arrive nearly 1 h too early. For s-level models at this resolution, the bathymetry

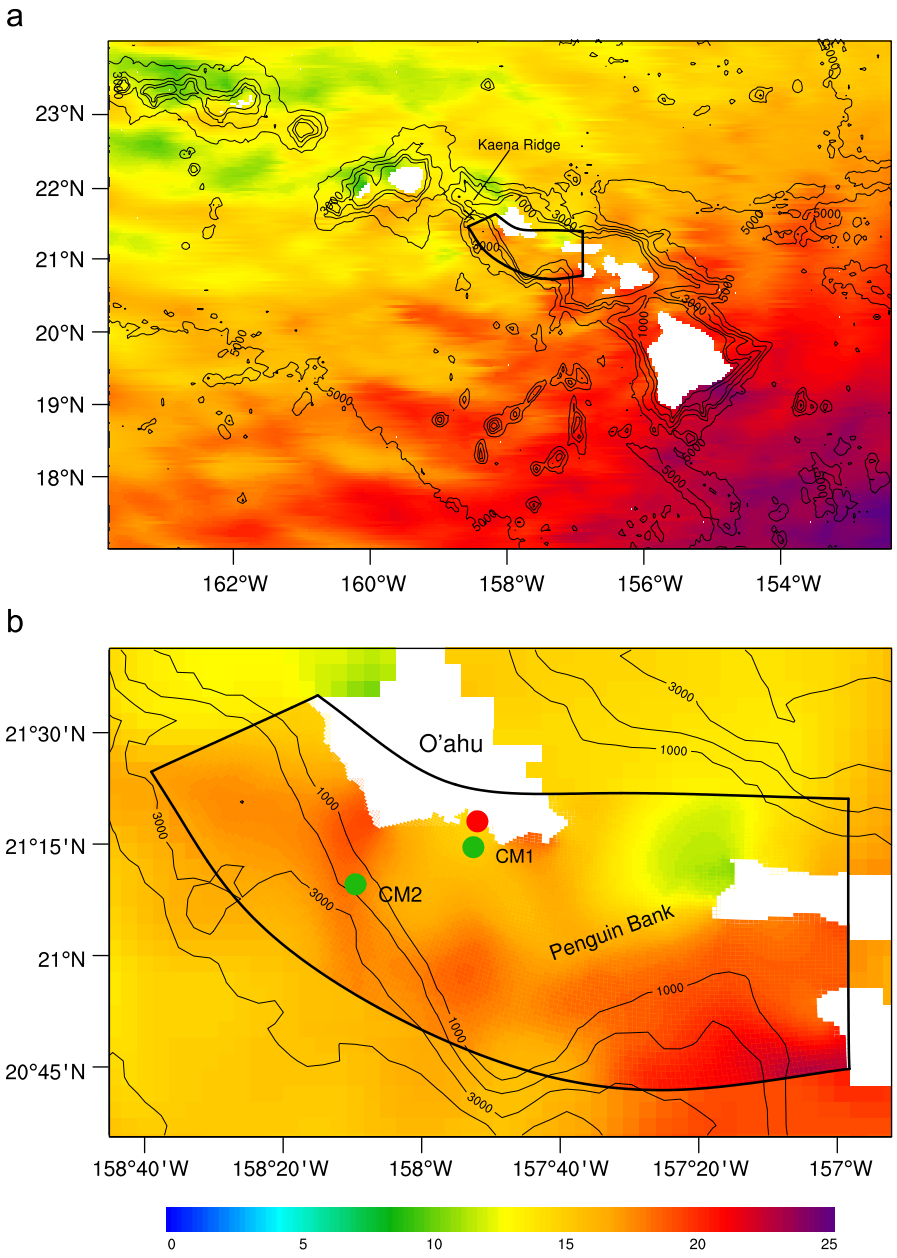

Fig. 5. M_2 free surface tidal amplitude (cm) for parent solution (a) with thick black line tracing child domain. The same but for the C180t case (b) with marked Honolulu tide gauge station (red dot) and current meter moorings CM1-2 (green dots). Bathymetry contour interval is 1000 m. (For interpretation of the references to color in this figure legend, the reader is referred to the web version of this article.)

Table 1
M_2 amplitudes (cm) and phases (degrees) with appropriate error estimates of tidal fit along with *D*-distance (cm) defined between different numerical experiments and Honolulu tide gauge station values.

Case	Amplitude	Amp. error	Phase	Phase error	Distance *D*
Honolulu	16.62	2.57	54.31	10.35	
Carter et al. (2008)	16.50	–	57.00	–	0.79
Parent	13.96	0.04	25.38	0.20	8.06
C60	13.87	0.12	61.92	0.50	3.41
C180	11.62	0.09	59.80	0.41	5.17
C180t	14.31	0.10	58.88	0.38	2.62

cannot be made shallower due to the increase in horizontal pressure-gradient errors (Shchepetkin and McWilliams, 2003). For comparison, we present the results from Carter et al. (2008) to compare a four times greater resolution, tidal only model (without nesting, etc.) that neglects the impact of horizontal pressure-gradient errors. Therefore, it is crucial to nest a child model to better resolve the complex bathymetry along the island slope and to impose the tides at the boundaries in an appropriate matter. Table 1 reveals that even with the fixed frequency BC, the higher resolution child model improves the comparison with the tide gauge. The distance, *D*, is improved by 57% in the C60 case, 36% in the C180 case, but by 67% in the C180t case. As before, although the C180 minute case was used to fit the tidal harmonics, specifying the harmonics separately yields a superior solution. One should note that the large estimate of tidal fit phase error in the observed tide gauge M_2 is probably due to the spreading of the M_2 spectrum on surrounding frequencies as a product of nonlinear interactions of other tidal constituents, bottom friction, nonlinear dynamics as well internal waves (Colosi and Munk, 2006). Taking the estimate of tidal fit error into account, the C180t model

solution is well within the observed tidal fit error limit for both amplitude and phase. Thus, using locally derived, coarse barotropic and baroclinic tides can provide the proper forcing for a high resolution model. Although the coarse model was out-of-phase with the tide-gauge, it is in the proper phase along the deeper boundaries of the nest, and the child propagates the signal onto the proper bathymetric shelf slowing to arrive at the appropriate time.

The barotropic tidal analysis is not surprising given the results of the previous section; however, of more concern are the dynamics of the tidally induced baroclinic internal waves. The use of the ADCP observations provides significant value in comparing the baroclinic results from the different cases. The baroclinic tides propagate at the same frequency as the barotropic tide; however, for a single location, there is a quasi-random phase-shift that occurs due to changes in oceanic density that affect the propagation of the baroclinic wave (Chavanne et al., 2010). We compare the two differing mooring locations with the child and parent models to quantify the effects of the BC.

The CM1 data were collected during Mamala Bay Experiment from June 1996 through July 1997 (http://stellwagen.er.usgs.gov/mamala_bay.html) predominantly in the bottom layer in an experiment to quantify sediment transport. For each depth of the current observations, the M_2 tidal ellipse is computed for the time period over which the data are available. Similarly, the tidal ellipse is computed for each vertical layer of the models, with comparisons of the three ellipse components shown in Fig. 6. As seen in the figure, there is a problem with the 370 m observed currents as the inclination fit error is nearly as large as the full spectrum. It is evident that parent model is having trouble in predicting the correct major tidal semi-axes and inclination. The baroclinic amplitude is nearly 25 cm/s and is significantly higher than the observed values. The bathymetry is actually shallower in the parent grid by nearly 50 m; however, the island slope is less steep and deeper, which would allow stronger signals to amplify on the slope. On the other hand, child solutions tend to follow the same vertical structure having different solutions at the bottom layers where we have observations to compare with. RMSE values between model cases (C60, C180, C180t, parent) and observations (without suspicious one) for major ellipse parameter are 6.3, 2.5, 1.5 and 15.9 cm/s. In the case of minor ellipse axes 0.7, 0.7, 0.5, 0.4 cm/s, respectively. Interesting to note is that C60 case (red curve at Fig. 6) predicts tidal velocities stronger and further away from observed one, similar to the parent solution and opposite to the C180 and C180t simulations. In that case Mean Error for major ellipse axes is showing bias between model and observations having values 6, −2, −0.5 and 16 cm/s, respectively. This is probably due to more frequent BC update than in the C180 case that constrain the child integration closer to parent system.

On the other hand, the CM2 ADCPs were deployed to sample the upper water column south, southwest tip of O'ahu from May 2010 to December 2010 using 105 vertical cells 10 m thick (Fig. 7). Tidally analyzed velocities agree well when compared with modeled tidal

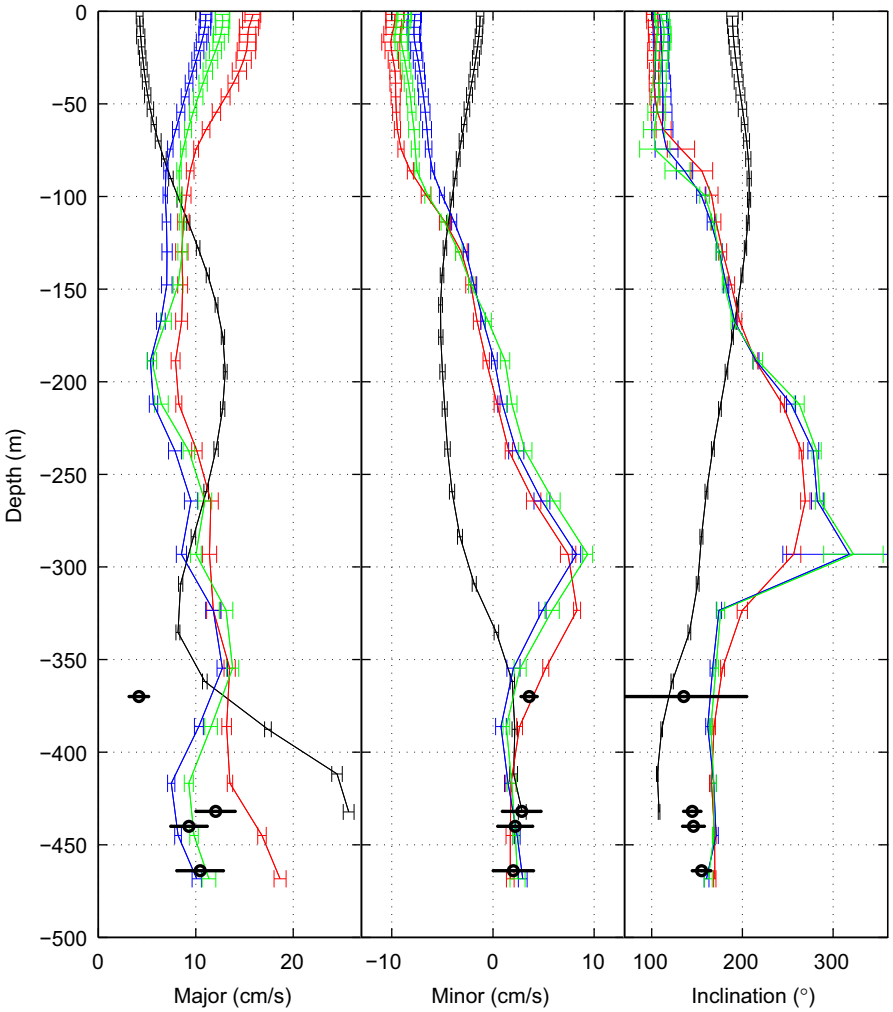

Fig. 6. CM1 current meter and model M_2 tidal ellipse parameters with appropriate tidal fit errors for parent (black), C60 (red), C180 (blue) and C180t (green) solutions. Observations are marked with black circles. (For interpretation of the references to color in this figure legend, the reader is referred to the web version of this article.)

ellipse parameters. The child solutions exhibit higher variability in each parameter as compared to the parent. Tidal ellipse inclination is better resolved by the various child cases, illustrating that topographic steering of the flow is more improved by the higher model grid resolution. Reduction in major tidal ellipse parameter from the surface down to 150 m depth is adequately captured inside all cases; however, the increase at the 380 m depth is missing from all models. The child cases at the depth show decreased major ellipse axes while at the same time having increased minor ellipse values giving less polarized tidal ellipses, as found in observations. RMSE values for major tidal ellipse, in the same order as for CM1, are 2.0, 2.9, 2.3 and 1.8 cm/s while for minor ellipse axes 2.8, 2.8, 2.8 and 1.8 cm/s. Based on those values parent solution is the closest one to the observations, however overall differences between model solutions are not so pronounced as in the CM1 case.

Overall, in comparing the M_2 solutions with observed data for both current meter stations and Honolulu tide gauge station, we find that method (ii) C180t case is the most consistent with the observed tidal structure. The importance of these comparisons is that the observations capture both the baroclinic and barotropic signals, and that the properly prescribed BC (via C180t) are able to best approximate the observed values.

As with the idealized case, we also aim to compare the baroclinic energy flux. We show the baroclinic energy flux for each vertical column in the model grid in Fig. 8 for three cases C60, C180, and C180t. All three figures are consistent with the results of Carter et al. (2008) with the strongest energy flux found on the western side of O'ahu directed from Kaena Ridge (northwest of O'ahu, Fig. 5) to the south, southeast with magnitudes of 10–12 kW/m. The southern section of O'ahu is characterized with smaller values (2 kW/m) following the isobaths to the west. As with the idealized case, lowering the frequency of the BC will decrease the amount of baroclinic tidal energy, and that some of this can be mitigated by method (ii). Comparing the total fluxes from Fig. 8, we find that C180 is 23.8% lower than C60 while C180t is actually 4.5% stronger than C60 case.

As before, we use the total kinetic energy to examine the significance of a slight change in baroclinic energy flux. Unlike the

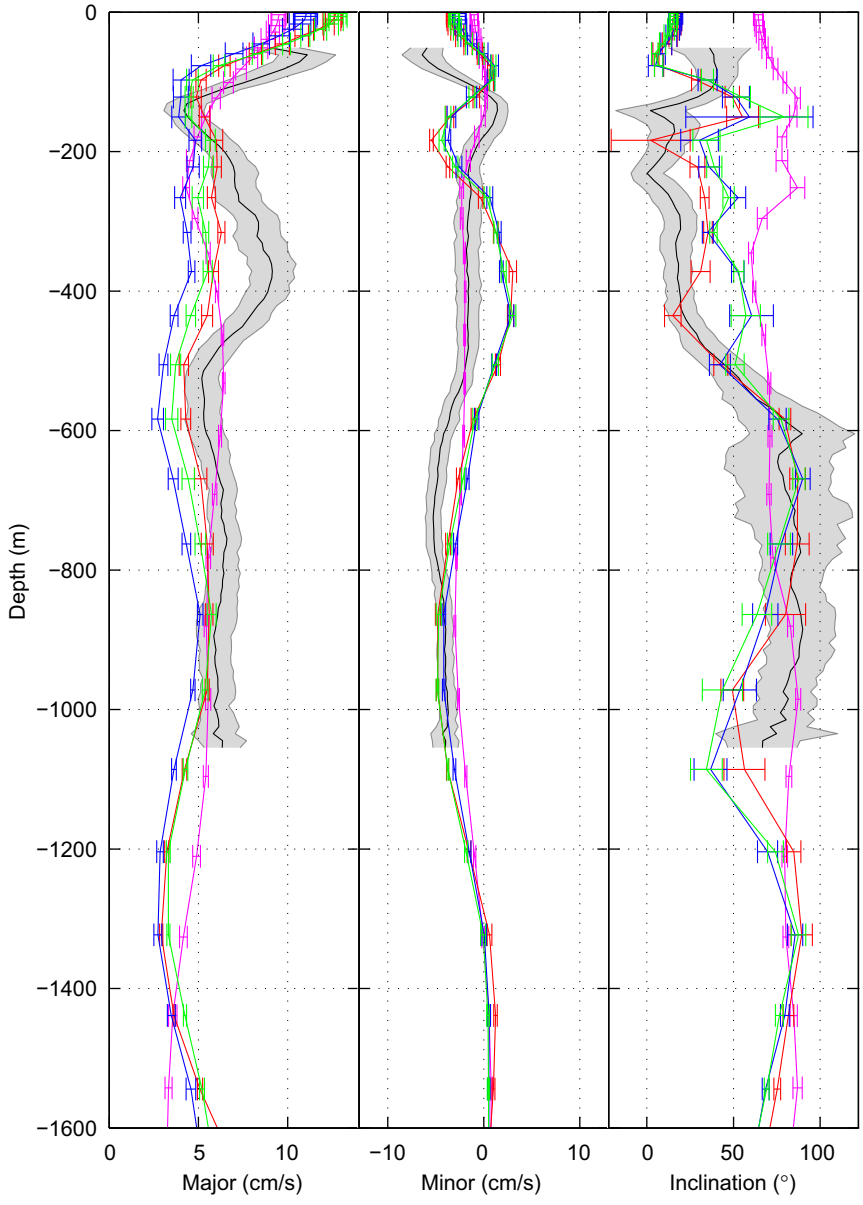

Fig. 7. CM2 ADCPs (black) and model M_2 tidal ellipse parameters with appropriate tidal fit errors for parent (magenta), C60 (red), C180 (blue) and C180t (green) solutions. (For interpretation of the references to color in this figure legend, the reader is referred to the web version of this article.)

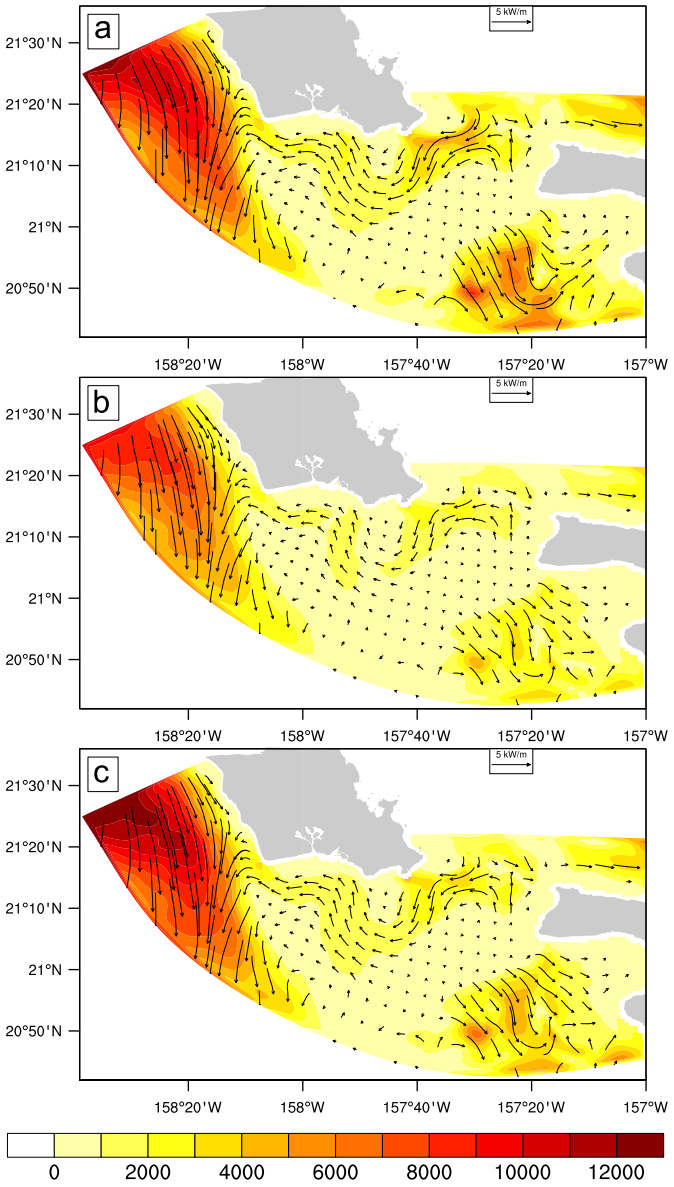

Fig. 8. Baroclinic energy flux for different child model cases; C60 (a), C180 (b), and C180t (c).

idealized experiment, we will compare the total kinetic energy to the C60 case because the parent and child are significantly different in terms of their bathymetry and yield quite different tidal solutions (see for example Honolulu tide gauge comparison). The C180 (C180t) case reduces the total kinetic energy of the C60 case by 29% (5%). However, if we examine only the barotropic M_2 tidal energy, we find that C180 reduces the energy by 10% while C180t increases the energy by 10% showing that the M_2 amplitudes are stronger in C180t than C60. This is expected as we are comparing to the C60 case that undersamples the barotropic amplitude (as shown in Appendix).

If we examine the total potential energy rather than kinetic, then the results are not surprising given the above. C180 reduces the potential energy by 15% from C60, while C180t increases it by 2%. Thus C180 underestimates both kinetic and potential energy and more frequent BC should be used (e.g., C60). However, the optimal solution is to utilize the C180t case, which eliminates the tidal aliasing issues and provides the proper barotropic energy.

There is obvious benefit to nesting as each child case is characterized by fine bathymetry and high resolution in coastal regions capable of reproducing modified baroclinic energy flux. As shown, the 4 km is incapable of capturing the tidal interactions with the complex terrain, but it provides the proper baroclinic and barotropic tidal structure if specified via method (ii) for the child domain to properly resolve the tidal dynamics.

5. Discussion

Tides often play an important role in the circulation of coastal and shelf environments. In numerical modeling, high-resolution models are required for these regions, and specifying the proper tidal BC is crucial. We examined two methods for one-way nesting (i) specifying the parental values at specified interval; and (ii) using the same BC as (i), but extracting the barotropic tides and specifying them back spectrally inside the model.

Comparing these methods in the simple idealized seamount case on f-plane, we showed that if BC are specified only through discrete time records, the baroclinic energy flux and total kinetic energy are both significantly underestimated (by $\sim$38% for C180), and that the barotropic tidal energy is aliased at higher frequencies due to the linear, temporal interpolation of the BC performed by most numerical models. However, using method (ii), the total kinetic energy was only slightly underestimated with the loss coming from an 11% reduction in the baroclinic energy flux as compared to C20.

For the idealized seamount with advective flow on a β-plane, method (ii) showed dramatic improvements over the standard, method (i) cases. The total kinetic energy was similar between the C20 and C180t cases with little loss in baroclinic energies. The EKE was maintained across both; however, the C180t has the advantage of avoiding aliased energy as well as a great reduction (factor of 9) in space requirements.

To examine a realistic case, the Hawaiian archipelago is a strong barotropic to baroclinic conversion region and serves as ideal test bed for our analysis. Using a child model near Island of O'ahu, characterized with variable spatial resolution (500 m in a coastal region to 2500 m in deep part) and nested into 4 km Hawai'i regional model providing BC, we found results consistent with the idealized cases. Comparison with tide gauge station in Honolulu yield superior results for method (ii) case having the smallest model to observation differences. Verifying vertical current structure using two different ADCP mooring lines showed again favorable results for method (ii). Baroclinic energy flux for nested model domain gave expected results capturing well known patterns (Carter et al., 2008). Differences between C60, C180 and C180t in terms of total baroclinic flux yield $\sim$24% reduction for C180 and increase of 4.5% for C180t when compared against C60 case. The results showed that C180 case dramatically reduces the total kinetic energy (30%) while C180t increase nearly 5% with respect to C60 case. In terms of total potential energy C180 case reduces it for 15% while C180t increases by 2% of those in C60 case.

As we saw from our experiments there are many benefits of using method (ii), specifically the C180t case, when specifying BC from parent to child in one-way nesting system such as

1. using a parent grid to properly resolve barotropic tides and generate baroclinic tides not resolved by global tidal models,
2. propagating the correct barotropic component of energy from parent to child model,
3. eliminating the aliasing at higher energy frequencies due to linear interpolation of BC on model time steps,
4. keeping similar EKE, total kinetic and potential energy as in parent solution,
5. separating deterministic tidal part from BC as favorable way in data assimilation studies,

6. significant reduction in computer storage resource requirements by avoiding frequently saving of parent fields.

As method (ii) only specifies the barotropic tides spectrally, it is important that the proper sampling frequency of the parent be chosen for the BC to capture the baroclinic structure. We found that for the two domains shown (idealized and Hawai'i), 3 h sampling did not result in a significant loss of baroclinic energy; however, this choice would be made for each domain. For the barotropic component, BC of at least 6 h are required for fitting the semidiurnal tides to the tide.

Although presented only in the one-way nesting case, these results are partly applicable to two-way nesting schemes. As these schemes often do not provide BC at each time-step, the aliasing problem would be present, and an appropriate period for BC exchange must be accounted for in the two-way schemes. However, in that system child solution is propagating information back into the parent one so the method (ii) seems inappropriate for computing spectral part in advance.

Furthermore, the methods shown in this paper are relevant to any shelf and slope region in which tides play a fundamental component of the circulation.

Acknowledgements

Authors would like to thank to Glenn Carter, Rob Hall, and Mark Merrifield for discussions regarding internal tides, Richard Signell and USGS who kindly made available CM1 current meter data, Todd Ericksen and Sound and Sea Technology for CM2 data, and University of Hawai'i Sea Level Center for Honolulu tide gauge data. Dr. Janeković was supported by NOAA Grant NA10NOS4730016 and Dr. Powell was supported by The Office of Naval Research Grant #N00014-09-10939. We are grateful to comments by the reviewers which led to substantial improvements in the manuscript. University of Hawai'i at Mānoa, School of Ocean and Earth Science and Technology Contribution Number 8508.

Appendix A. Sampling BC and aliasing

The Nyquist sampling frequency is fundamental to discrete sampling theory and requires at least two samples per cycle to reconstruct a signal. However, even when the requirement is satisfied, aliasing can be introduced when interpolating between those samples. In order to illustrate the problem, we can construct sinusoidal signal at the exact M_2 period ($T_{M_2} = 12.42$ h) as

$$\mathcal{Y}(t) = \sin\left(\frac{2\pi}{T_{\mathcal{M}_2}}\, t\right) \tag{A.1}$$

with time vector t defined with step of 1 min. Of course, knowing the frequency and subsampling at least every 6.21 h, we can perfectly reconstruct the signal and this is why method (ii) can properly prescribe the barotropic tide.

The problem arises from linearly interpolating (as most ocean models do) between samples. To illustrate the problem, we sample the signal using sampling rates of 10 min, 1 h, 2, 3, 4, and 6 h (Fig. A1) which all satisfy Nyquist–Shannon sampling criteria; hence, there is no aliasing introduced from subsampling the signal. In compressing audio signals, it is well-known to use piecewise linear approximation such that amplitude and frequency envelopes are "downsampled". A set of breakpoints are defined in time between which linear segments were used. These breakpoints correspond to "knot points" in the context of the interpolation.

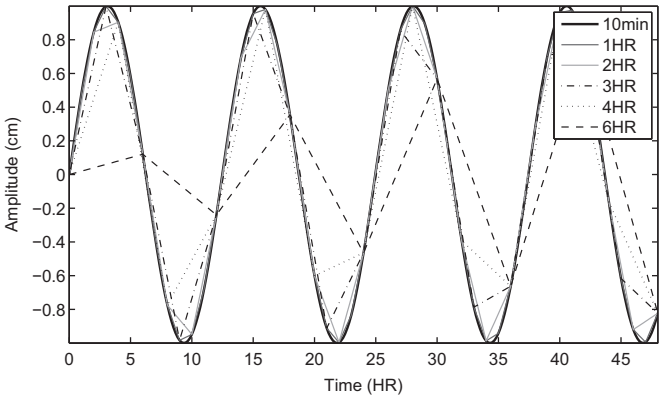

Fig. A1. M_2 tidal signal and linearly interpolated subsampled signals back on the original time vector.

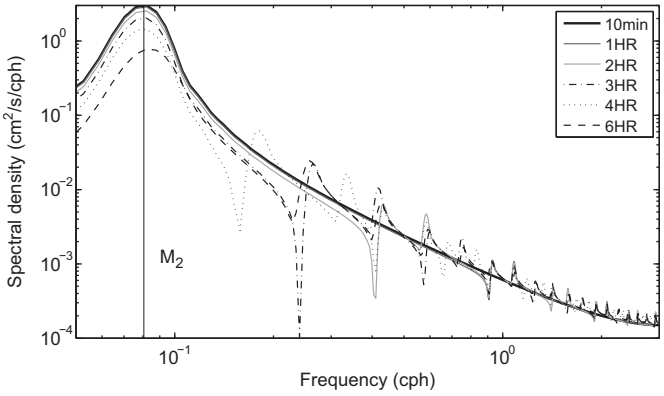

Fig. A2. Power spectral density of subsampled and then linearly interpolated signals back on the original time vector.

In the present case, we linearly interpolate from those sampled values ("knot points") back onto the original time vector t (note that we are now using only discrete subsampled values for the interpolation and that there is no reduction in size because we are interpolating back on original time vector t), as seen in Fig. A1. This emulates the approach of the ROMS model in handling the BC in time. In this way, the specified BC are no longer piecewise smooth functions in time, but a discrete set of lines joined at sampled points.

Examining the spectral signature of these interpolated signals show that (as evident in Fig. A1) the amplitudes are reduced at lower frequency sampling, but as shown in Fig. A2, the linear interpolation introduces aliased energies at even multiples of higher frequencies. As the subsampling frequency decreases, the aliasing frequencies increase.

Saving the parent model fields at discrete time intervals is justified only when using method (ii) to compute the spectral tidal information (which, actually fits the analytic signal function to the samples), and use the function inside the model to reconstruct the barotropic tidal variability at every model time-step. Using only linear interpolation in between sampled points, introduces unacceptable spectral aliasing (at lower sampling rates) and greatly reduced amplitudes.

References

Balmforth, N.J., Peacock, T., 2009. Tidal conversion by supercritical topography. Journal of Physical Oceanography 39, 1965–1974.

Bennett, A.F., 1992. Inverse Methods in Physical Oceanography. Cambridge University Press, Cambridge 346 pp.

Bennett, A.F., Kloeden, P.E., 1978. Boundary conditions for limited-area forecasts. Journal of the Atmospheric Sciences 35, 990–996.
Carter, G.S., Merrifield, M.A., Becker, J., Katsumata, K., Gregg, M.C., Luther, D.S., Levine, M.D., Boyd, T.J., Firing, Y.L., 2008. Energetics of M_2 barotropic–tobaroclinic tidal conversion at the Hawaiian Islands. Journal of Physical Oceanography 38, 2205–2223.
Chapman, D.C., 1985. Numerical treatment of cross-shelf open boundaries in a barotropic coastal ocean model. Journal of Physical Oceanography 15, 1060–1075.
Chavanne, C., Flament, P., Luther, D.S., Gurgel, K.W., 2010. The surface expression of semidiurnal internal tides near a strong source at Hawaii. Part II. Interactions with mesoscale currents. Journal of Physical Oceanography 40, 1180–1200.
Colosi, J.A., Munk, W., 2006. Tales of the venerable Honolulu tide gauge. Journal of Physical Oceanography 36, 967–996.
Debreu, L., Blayo, E., 2008. Two-way embedding algorithms: a review. Ocean Dynamics, 415–428 (Special Issue on Multi-Scale Modelling: Nested Grid and Unstructured Mesh Approaches).
Dinniman, M.S., Klinck, J.M., 2002. The influence of open versus periodic alongshore boundaries on circulation near submarine canyons. Journal of Atmospheric and Oceanic Technology 19, 1722–1737.
Egbert, G.D., Erofeeva, S.Y., 2002. Efficient inverse modeling of barotropic ocean tides. Journal of Atmospheric and Oceanic Technology 19, 183–204.
Evensen, G., 1994. Sequential data assimilation with a non-linear quasi-geostrophic model using Monte Carlo methods to forecast error statistics. Journal of Geophysical Research 99, 10,143–10,162.
Garrett, C., Kunze, E., 2007. Internal tide generation in the deep ocean. The Annual Review of Fluid Mechanics 39, 57–87.
He, R., Wilkin, J.L., 2006. Barotropic tides on the southeast New England shelf: a view from a hybrid data assimilative modeling approach. Journal of Geophysical Research 111, C08002.
Janeković, I., Kuzmić, M., Bobanović, J., 2003. The Adriatic Sea M_2 and K_1 tides by 3D model and data assimilation. Estuarine, Coastal and Shelf Science 57, 873–885.
Janeković, I., Sikirić, M.D., 2007. Improving tidal open boundary conditions for the Adriatic Sea numerical model. Geophysical Research Abstracts 9, 03217.
Le Dimet, F., Talagrand, O., 1986. Variational algorithms for analysis and assimilation of meteorological observations: theoretical aspects. Tellus 38A, 97–110.
Lorenzo, E.D., Young, W.R., Smith, S.L., 2006. Numerical and analytical estimates of M_2 tidal conversion at steep oceanic ridges. Journal of Physical Oceanography 36, 1072–1084.
Marchesiello, P., McWilliams, J.C., Shchepetkin, A.F., 2001. Open boundary conditions for long term integration of regional oceanic models. Ocean Modelling 3, 1–20.
Mason, E., Molemaker, J., Colas, A.F.S.F., McWilliams, J.C., Sangrà, P., 2010. Procedures for offline grid nesting in regional ocean models. Ocean Modelling 35 (1–2), 1–15.
Merrifield, M.A., Holloway, P.E., 2002. Model estimates of M_2 internal tide energetics at the Hawaiian Ridge. Journal of Geophysical Research 107, 3179.
Nash, J.D., Alford, M.H., Kunze, E., 2005. Estimating internal wave energy fluxes in the ocean. Journal of Atmospheric and Oceanic Technology 22, 1551–1570.
Oddo, P., Pinardi, N., 2008. Lateral open boundary conditions for nested limited area models: a scale selective approach. Ocean Modelling 20, 124–156.
Oliger, J., Sundstrom, A., 1978. Theoretical and practical aspects of some initial boundary value problems in fluid mechanics. The SIAM Journal on Applied Mathematics 35, 419–446.
Palma, E.D., Matano, R.P., 1998. On the implementation of passive open boundary conditions for a general circulation model: the barotropic model. Journal of Geophysical Research 103, 1319–1341.
Pawlowicz, R., Beardsley, B.B., Lentz, S., 2002. Harmonic analysis including error estimates in MATLAB using T_TIDE. Computers and Geosciences 28, 929–937.
Penven, P., Debreu, L., Marchesiello, P., McWilliams, J.C., 2006. Evaluation and application of the ROMS 1-way embedding procedure to the central California upwelling system. Ocean Modelling 12, 157–187.
Qian, H., Shaw, P.T., Ko, D.S., 2010. Generation of internal waves by barotropic tidal flow over a steep ridge. Deep-Sea Research I 57, 1521–1531.
Shchepetkin, A.F., McWilliams, J.C., 2003. A method for computing horizontal pressure-gradient force in an oceanic model with a nonaligned vertical coordinate. Journal of Geophysical Research 108 (C3) 34 pp.
Shchepetkin, A.F., McWilliams, J.C., 2005. The regional oceanic modeling system: a split-explicit, free-surface, topography-following-coordinate ocean model. Ocean Modelling 9, 347–404.
Shchepetkin, A.F., McWilliams, J.C., 2009. Correction and commentary for ocean forecasting in terrain-following coordinates: formulation and skill assessment of the regional ocean modeling system by Haidvogel et al., J. Comput. Phys. 227, pp. 3595–3624. Journal of Computational Physics 228, 8985–9000.
Simmons, H.L., Hallberg, R.W., Arbic, B.K., 2004. Internal wave generation in a global baroclinic tide model. Deep-Sea Research II 51, 3043–3068.
Xie, S.-P., Liu, W., Liu, Q., Nonaka, M., 2001. Far-reaching effects of the Hawaiian islands on the pacific ocean-atmosphere system. Science 292 (5524), 2057–2060.
Zaron, E.D., Egbert, G.D., 2006. Estimating open-ocean barotropic tidal dissipation: the Hawaiian Ridge. Journal of Physical Oceanography 36, 1019–1035.